Physics of Plasmas

Direct observation of the non-locality of non-diffusive counter-gradient electron thermal transport during the formation of hollow electron-temperature profiles in the Large Helical Device

Cite as: Phys. Plasmas **29**, 032504 (2022); https://doi.org/10.1063/5.0074351
Submitted: 08 October 2021 • Accepted: 01 February 2022 • Published Online: 02 March 2022

T. I. Tsujimura, T. Kobayashi, K. Tanaka, et al.

ARTICLES YOU MAY BE INTERESTED IN

Physics of Plasmas ARTICLE scitation.org/journal/php

Direct observation of the non-locality of non-diffusive counter-gradient electron thermal transport during the formation of hollow electron-temperature profiles in the Large Helical Device

Cite as: Phys. Plasmas **29**, 032504 (2022); doi: 10.1063/5.0074351
Submitted: 8 October 2021 · Accepted: 1 February 2022 ·
Published Online: 2 March 2022

View Online Export Citation CrossMark

T. I. Tsujimura,[1,a)] T. Kobayashi,[1,2] K. Tanaka,[1,3] K. Ida,[1,2] K. Nagaoka,[1] M. Yoshinuma,[1] I. Yamada,[1] H. Funaba,[1] R. Seki,[1,2] S. Satake,[1,2] T. Kinoshita,[3] T. Tokuzawa,[1,2] N. Kenmochi,[1] H. Igami,[1] K. Mukai,[1,2] M. Goto,[1,2] and Y. Kawamoto[1]

AFFILIATIONS

[1]National Institute for Fusion Science, National Institutes of Natural Sciences, Toki, Gifu 509-5292, Japan
[2]The Graduate University for Advanced Studies, SOKENDAI, Toki, Gifu 509-5292, Japan
[3]Interdisciplinary Graduate School of Engineering Sciences, Kyushu University, Kasuga, Fukuoka 816-8580, Japan

[a)]Author to whom correspondence should be addressed: tsujimura.tohru@nifs.ac.jp

ABSTRACT

A heating source with off-axis electron cyclotron heating (ECH) alone produced a plasma with a quasi-steady-state hollow electron-temperature profile in the Large Helical Device. The clear formation of this quasi-steady-state hollow electron-temperature profile can be explained by adding the outward heat convection term to the diffusion term, as a simple model to describe the electron heat flux, using the energy conservation equation. In addition, we directly observed the non-locality of the non-diffusive (convective) contribution in transient electron thermal transport in the condition that power-modulated on-axis ECH was applied to the plasma sustained by off-axis ECH. The experimentally evaluated flux-gradient relation shows two different positive values of the electron heat flux at zero temperature gradient by going back and forth between positive and negative temperature gradient regions in the transport hysteresis phenomenon.

I. INTRODUCTION

The simplest diffusion model has been used to understand plasma transport, e.g., integrated transport modeling and scaling, internal transport barriers (ITBs), etc., using the gyro-Bohm diffusion coefficient.[1–8] However, recent studies have reported that the diffusion process is insufficient for several cases, e.g., non-local cold pulse propagation, the off diagonal term (convection), transport hysteresis phenomena, etc.[9–17] Some of them are being solved by detailed modeling of turbulence, but there are still some unresolved issues.

Regarding heat convection, some experimental observations have been reported in tokamaks. During localized off-axis electron cyclotron heating (ECH), inward electron heat convection is required to explain steady-state peaked electron-temperature (T_e) profiles even in the absence of a central heating source.[18,19] On the other hand, in the case of far-off-axis ECH for the RTP tokamak, where the T_e profile becomes significantly hollow, the sustainment of a strong negative gradient on the electron temperature, i.e., $-\nabla T_e < 0$, can be explained by the presence of outward heat convection.[20] Hollow T_e profiles were also observed in old stellarators Heliotron-E and Wendelstein 7-AS in the case of off-axis ECH.[21,22]

However, several experimental observations have already revealed that transient responses of electron thermal transport can be explained by non-diffusive non-local properties.[12–15,23–26] Here, non-local electron thermal transport denotes that the electron heat flux q_e cannot be determined by transport coefficients of local plasma parameters, e.g., $-\nabla T_e$, T_e, etc. As a result, the transport hysteresis appears.

The flux-gradient diagram shows a hysteresis trajectory, where q_e rapidly changes in response of heating, while $-\nabla T_e$ continuously changes. The transport hysteresis phenomena do not clearly follow the local diffusion model, where q_e is determined by local $-\nabla T_e$ with the diffusion coefficient alone. Although inward/outward electron heat convection can describe some steady-state T_e profiles, the direct observations of the relation between q_e and $-\nabla T_e$ are required to study transient transport properties without assuming a specific transport model. In this paper, we reproduce the formation of a quasi-steady-state hollow T_e profile in the Large Helical Device (LHD). Then, we discuss for the first time the direct observation of the non-locality of the non-diffusive contribution in transient electron thermal transport, which is associated with outward electron heat convection, through the experimental evaluation of the flux-gradient relation as well as the flux-temperature relation.

II. EXPERIMENTAL SETUP

A. LHD experiments

Plasma experiments to study hollow T_e profiles were performed in the LHD.[27] The confinement magnetic field configuration was set to be the standard one in the LHD. The magnetic field strength was set to be $B_t = 2.75$ T at the magnetic axis of $R_{ax} = 3.6$ m. The electron cyclotron (EC) resonance layer at 2.75 T, for the second-harmonic extraordinary (X2) mode at 154 GHz, ranges from the magnetic axis to the plasma edge so that the deposition location can be scanned radially.

Two types of experiments were performed in this study. The first one was to form a hollow T_e profile at a quasi-steady state. A deuterium plasma started up with on-axis ECH from 3.0 to 3.3 s, followed by the main heating source to sustain the plasma from 3.3 to 4.8 s with X2-mode ECH along with a 154-GHz gyrotron with its injection power of 0.80 MW from the 2-OUL launching antenna, which is installed at the outer port on the horizontally elongated plasma cross section. The deposition location of the X2-mode ECH was radially scanned on a shot-to-shot basis to see the change of quasi-steady-state T_e profiles. The pulse width of 1.5 s is longer than a typical energy confinement time of a few hundred ms in ECH plasmas.[28] The second type of experiment was a modulation ECH (MECH) experiment, where on-axis MECH was superimposed on off-axis ECH to excite the heat pulse propagation from the plasma center to the edge to observe the non-locality of the non-diffusion term directly. On-axis ECH was used to start up a deuterium plasma from 3.0 to 3.3 s. Then, on-axis MECH was deposited at $r_{eff} \simeq 0.1$ m with its injection power of 0.72 MW from the 2-OLL antenna, which is also installed at the outer port on the horizontally elongated cross section. Here, r_{eff} denotes the effective minor radius.[29] The MECH frequency was set at 2 Hz. The steady-state off-axis ECH was deposited at $r_{eff} \simeq 0.3$ m with its injection power of 0.80 MW from the 2-OUL launching antenna. Their gyrotron frequency was 154 GHz for X2-mode heating. Both pulse widths were set at 1.5 s from 3.3 to 4.8 s. ECH power deposition profiles were calculated by the ray-tracing code "LHDGauss."[30]

The radial profiles of T_e and n_e were measured with the Thomson scattering (TS) diagnostics.[31] The T_e profile was also measured with the high-time-resolution electron cyclotron emission (ECE) radiometer system.[32] The line-averaged electron density $\bar{n}_e$ was measured with the far-infrared laser interferometer.[33] The T_i profile was measured with charge exchange spectroscopy (CXS)[34] with 20 ms short-pulse diagnostic perpendicular neutral beam injection (NBI) triggered at 4.7 and 6.5 s only in both types of experiments. Since the NBI power over 4.5 MW is much larger than the ECH power less than 1 MW in the LHD, the NBI affects the plasma heated by ECH alone. Thus, the short-pulse NBI for the T_i measurement was applied only at 4.7 s near the end of the ECH pulse at 4.8 s. Then, another ECH was applied from 4.8 to 5.1 s, followed by tangential NBI from 5.1 s for the MECH experiment. The tangential NBI phase was used to calibrate the ECE signal intensity by T_e measured with TS. The central ion temperature T_{i0} was also measured with a crystal spectrometer.[35] Line-integrated radiation power was measured with resistive bolometer arrays.[36] The effective ion charge Z_{eff} was obtained by the visible Bremsstrahlung profile measurement,[37] and its radially constant value was used for analysis.

B. Dynamic transport analysis

The second type of experiment for direct observation of the non-locality of the non-diffusion term is illustrated in Fig. 1. This figure shows the schematic diagrams of radial profiles of T_e during on-axis MECH superimposed on off-axis ECH to excite heat pulse propagation and also shows the flux-gradient relation when the non-locality of the non-diffusive transport is present. The electron heat flux q_e is evaluated at the radius between the two deposition radii. In our case, the observation location is $r_{eff} \simeq 0.2$ m between the on-axis ECH location and the off-axis ECH location. Dynamic transport analysis to evaluate q_e even at the region of the negative $-\nabla T_e$ will show the transport hysteresis, where the different q_e is observed between the turn-on phase and the turn-off phase during on-axis MECH. On-axis MECH supplies finite positive q_e transiently flowing against the counter-gradient region. In contrast to the case of a steady-state hollow T_e profile, where net $q_e = 0$ at the region of $-\nabla T_e \leq 0$, due to no on-axis ECH, the transient transport phenomenon by on-axis MECH gives net $q_e > 0$ at the region of $-\nabla T_e \leq 0$. This transient counter-gradient transport cannot be explained by the local diffusion model. In addition, the transport hysteresis, including the region of $q_e > 0$ and $-\nabla T_e < 0$, cannot be explained by the local diffusion-convection model. Here, we regard the non-diffusion term as what gives rise to positive q_e even at zero $-\nabla T_e$.

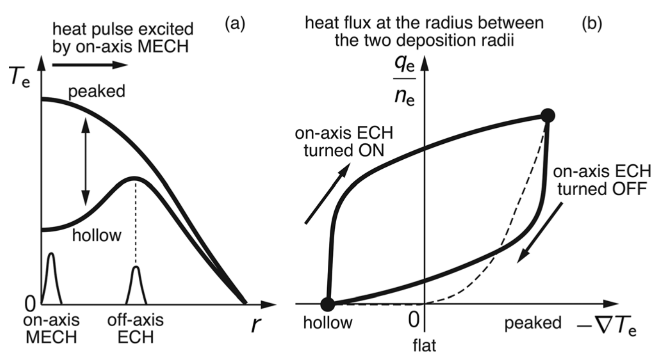

FIG. 1. Schematic diagrams of (a) radial profiles of T_e during on-axis MECH superimposed on steady-state off-axis ECH and (b) the flux-gradient relation when the non-locality of non-diffusive counter-gradient transport is present.

III. EXPERIMENTAL RESULTS

A. Formation of a quasi-steady-state hollow electron temperature profile

The first type of experiment to form a quasi-steady-state hollow T_e profile was performed. Similarly, in other devices where hollow T_e profiles were observed, a heating source with off-axis ECH alone exhibited the clear formation of a hollow T_e profile in the LHD. Figure 2 shows radial profiles of the ECH deposition power density P_{ECH}, the electron temperature T_e, the ion temperature T_i, and the electron density n_e in the cases of on-axis ECH, mildly off-axis ECH, and off-axis ECH. Here, $r_{eff} = a_{99} = 0.62$ m is the minor radius in which 99% of the electron stored energy is confined. The TS measurement data were at 4.667 s just before the diagnostic NBI pulse at 4.7 s for the CXS measurement to dismiss the effect of NBI heating on T_e. The results show that the peaked T_e profile changed to hollow by changing the deposition location outward on a shot-to-shot basis, while the T_i and n_e profiles were almost unchanged in these three discharges. After n_e adjustment by deuterium gas puffing, hollow T_e profiles were sustained during $\sim 3\tau_E$ in the off-axis ECH case, where τ_E denotes the energy confinement time, and it was estimated to be $\tau_E \sim 0.28$ s.

The quasi-steady-state hollow T_e profile in the LHD can be explained by adding the convection term to the diffusion term as a simple model to describe q_e given by

$$q_e(r) = -n_e\chi_e\frac{\partial T_e(r)}{\partial r} + n_eU_eT_e(r), \tag{1}$$

where χ_e and U_e denote the electron heat diffusivity and the electron heat convection velocity, respectively. The T_e profile can be derived semi-analytically from the steady-state energy conservation equation in the cylindrical coordinates as given by

$$0 = -\frac{1}{V'(r)}\frac{\partial}{\partial r}\left[V'(r)q_e(r)\right] + P_{ECH}(r),$$

when the following approximations can be met: the heating profile by Dirac's delta function $P_{ECH} \approx p\delta(r - r_{dep})$, the simple torus shape $V \approx 2\pi^2R_0r^2$ and $V' = 4\pi^2R_0r$, and radially constant χ_e, U_e, and n_e. Here, p is the heating power surface density, r_{dep} is the minor radius of the deposition location, R_0 is the major radius, and V' is the radial derivative of the plasma volume profile V. Then, the solutions are obtained as

$$\frac{\partial T_e(r)}{\partial r} = \begin{cases} \left(\frac{U_e}{\chi_e}\right)T_e & (r < r_{dep}), \\ \left(\frac{U_e}{\chi_e}\right)T_e - \frac{T_0}{r} & (r \geq r_{dep}), \end{cases} \tag{2}$$

$$T_e(r) = \begin{cases} T_{dep}\exp\left[\frac{U_e}{\chi_e}(r - r_{dep})\right] & (r < r_{dep}), \\ T_{dep}\exp\left[\frac{U_e}{\chi_e}(r - r_{dep})\right] + T_0\left[-E_i\left(\frac{U_e}{\chi_e}r_{dep}\right)\right. \\ \left. + E_i\left(\frac{U_e}{\chi_e}r\right)\right]\exp\left(\frac{U_e}{\chi_e}r\right), & (r \geq r_{dep}), \end{cases}$$

where E_i denotes the exponential integral function defined as $E_i(x) \equiv \int_x^\infty \frac{e^{-t}}{t}dt$ for $x > 0$. A parameter T_{dep} is the electron temperature at the deposition location r_{dep}. The other parameter T_0 is defined as $T_0 \equiv pr_{dep}/(n_e\chi_e)$.

A solid black line in Fig. 2(f) shows a curve fitted in Eq. (2) into the measured T_e data, where $R_0 = 3.6$ m, $r_{dep} = 0.32$ m, the

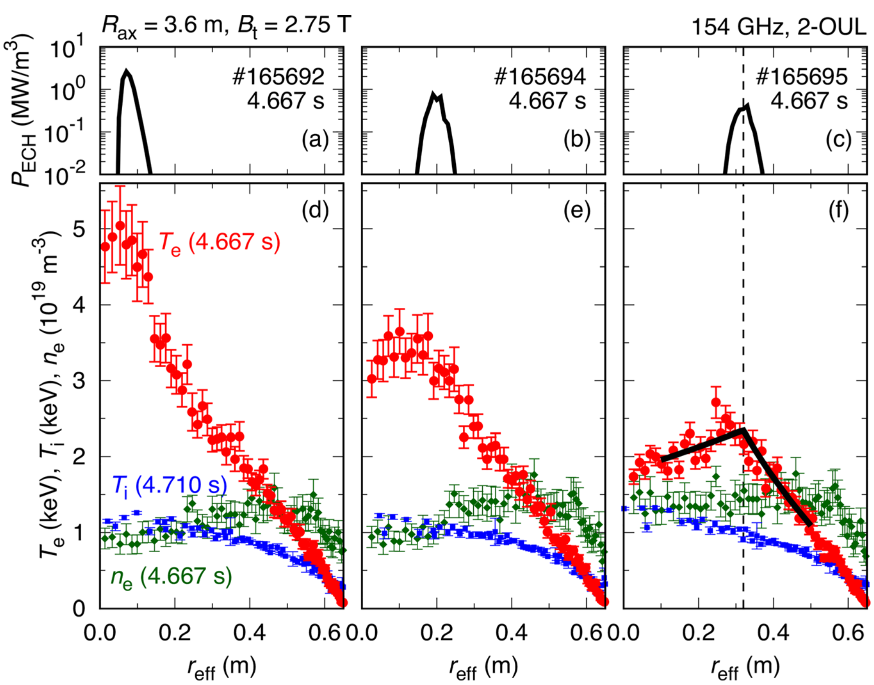

FIG. 2. Radial profiles of (a)–(c) ECH deposition power density P_{ECH}, (d)–(f) T_e, T_i, and n_e in cases of (a) and (d) on-axis ECH, (b) and (e) mildly off-axis ECH, and (c) and (f) off-axis ECH. Solid black line in (f) shows a curve fitted in Eq. (2) into measured T_e data.

volume-integral ECH absorption power is 0.78 MW, $p = 17\,\mathrm{kW/m^2}$, $T_{\mathrm{dep}} = 2.3$ keV, $T_0 = 3.4$ keV, $n_e = 1.4 \times 10^{19}\ \mathrm{m^{-3}}$, $\chi_e = 0.70\ \mathrm{m^2/s}$, and $U_e = 0.58$ m/s. The positive U_e means outward heat convection. The fitted curve with the modeled q_e in Eq. (1) precisely expresses the measured quasi-steady-state hollow T_e profile at reasonable values of χ_e and U_e in the LHD.[38] Figure 3 shows the radial profiles of the normalized electron heat flux q_e/n_e and the ratio between the diffusion term and the convection term by using the fitted curve. Inside the deposition radius of off-axis ECH, inward heat diffusion and outward heat convection cancel each other. Thus, the net electron heat flux is zero. Outside the deposition radius, more than 80% of q_e/n_e is accounted for outward heat diffusion. The contribution of outward heat convection is less than 20%.

B. Direct observation of the non-locality of the non-diffusion term

Although the simple model in Eq. (1), including outward heat convection, can describe some quasi-steady-state hollow T_e profiles, this model is insufficient to describe transient responses of electron thermal transport. For the second type of experiment, on-axis MECH was superimposed on steady-state off-axis ECH in the LHD. Figure 4 shows the time evolution of various quantities in a deuterium plasma discharge. The line-averaged electron density $\bar{n}_e$ was kept almost constant at $2 \times 10^{19}\ \mathrm{m^{-3}}$ during MECH. Along with Fig. 4, Fig. 5 shows the radial profiles of T_e and n_e during on-axis MECH. A peaked T_e profile was observed after on-axis MECH was turned on, while the T_e profile changed to a hollow one after on-axis MECH was turned off on the timescale of τ_E. On the other hand, the n_e profile was almost unchanged during MECH. In contrast to hollow T_e profiles, hollow n_e profiles are frequently observed in LHD plasmas produced by gas puffing. Particle transport in the particle source located at the peripheral plasma region has been discussed in the literature.[39,40] Here, the ECH-driven neoclassical particle flux is discussed in Appendix A. As shown in Fig. 4(d), the central ion temperature T_{i0} measured with CXS at 4.7 s was about 1 keV, which was close to T_{i0} that measured with a crystal spectrometer. In contrast to T_e, T_{i0} was almost unchanged regardless of on-axis MECH. Due to relatively low n_e, thermal relaxation from electrons to ions was much smaller than ECH power. Among resistive bolometer arrays for measuring the line-integrated radiation power, the sightlines with the minimum radius $r_{\mathrm{eff,min}} \simeq 0.5$ m and $r_{\mathrm{eff,min}} \simeq 0.05$ m are shown in Fig. 4(f). We observed that the radiation power on the sightline with $r_{\mathrm{eff,min}} \simeq 0.5$ m changed synchronously with MECH, while the radiation power on the sightline with $r_{\mathrm{eff,min}} \simeq 0.05$ m was almost unchanged during MECH. This difference is possibly

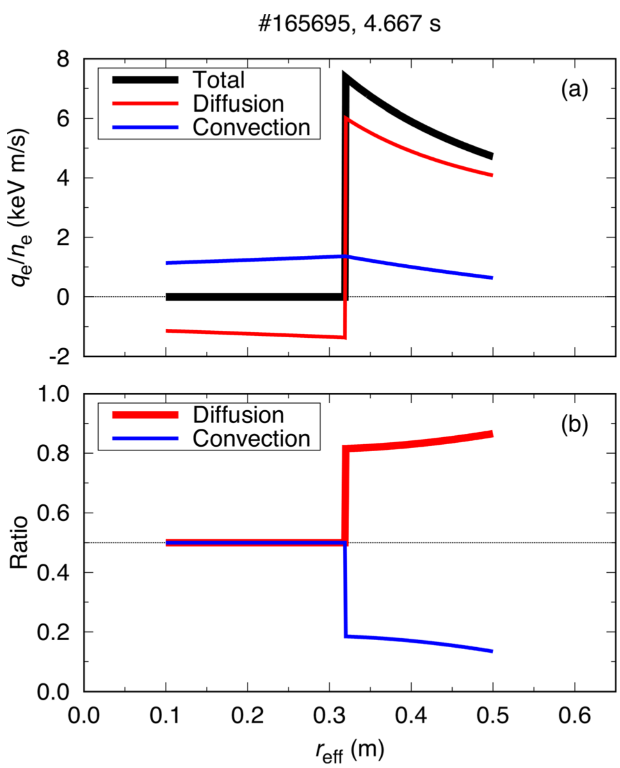

FIG. 3. Radial profiles of (a) q_e/n_e and (b) ratio between the electron heat diffusion and the electron heat convection.

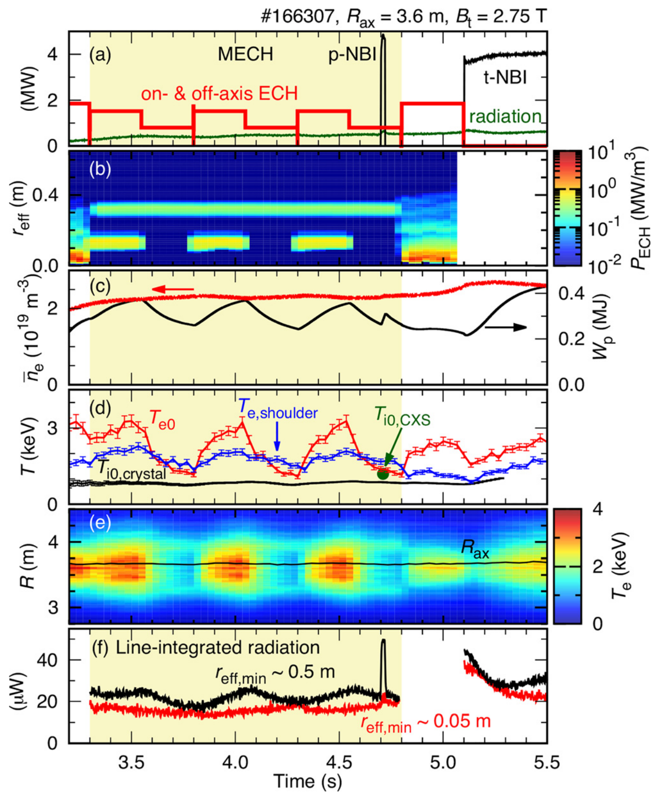

FIG. 4. Time evolution of the (a) injection power of ECH, port-through power of tangential NBI (t-NBI) and perpendicular NBI (p-NBI), radiation power, (b) radial profile of the ECH deposition power density P_{ECH}, (c) line-averaged density $\bar{n}_e$, plasma stored energy W_p, (d) central electron temperature T_{e0} at $R = 3.638$ m and $T_{e,\mathrm{shoulder}}$ at $R = 3.973$ m measured with TS, central ion temperature $T_{i0,\mathrm{CXS}}$ measured with CXS, $T_{i0,\mathrm{crystal}}$ measured with crystal spectrometer, (e) radial profile of T_e along with magnetic axis R_{ax}, and (f) line-integrated radiation power measured with resistive bolometer arrays, where minimum radius on each sightline is $r_{\mathrm{eff,min}} \simeq 0.5$ m and $r_{\mathrm{eff,min}} \simeq 0.05$ m. Time period of on-axis MECH is hatched in yellow.

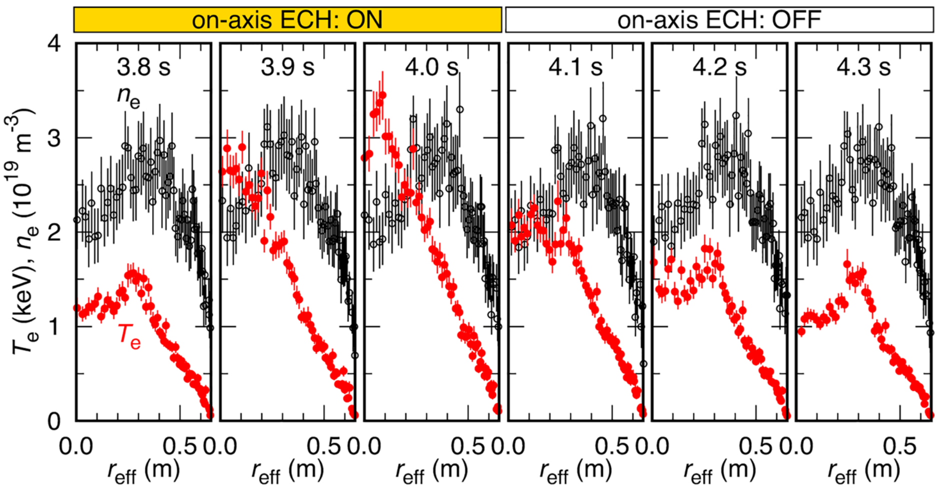

FIG. 5. Radial profiles of T_e and n_e during on-axis MECH.

caused by the larger line-integral volume around the plasma peripheral region in the sightline with $r_{eff,min} \simeq 0.5$ m than that in the sightline with $r_{eff,min} \simeq 0.05$ m. These results suggest that radiation loss is expected to be mainly concentrated at the plasma peripheral region, so that the radiation loss near the magnetic axis is much smaller than the on-axis ECH power density. By the way, the plasma stored energy W_p, as shown in Fig. 4(c), changed synchronously with on-axis MECH, but it decreased by 35% at most after turning off the on-axis MECH, which is discussed in Appendix B.

To discuss the flux-gradient relation, high-time-resolution T_e measured with the ECE diagnostic was calibrated by T_e measured with the TS diagnostic during the tangential NBI phase from 5.1 s, when all gyrotrons for ECH were turned off, where the effect of non-thermal electrons on ECE signals could be neglected.[41] Figure 6 shows the comparisons between T_e measured with ECE and T_e measured with TS for ECH and NBI phases. The measurement location of $r_{eff} = 0.21$ m is where the negative $-\nabla T_e$ is formed during only off-axis ECH, while $r_{eff} = 0.40$ m is outside the negative $-\nabla T_e$ region. The result shows that T_e measured with ECE is in good agreement with T_e

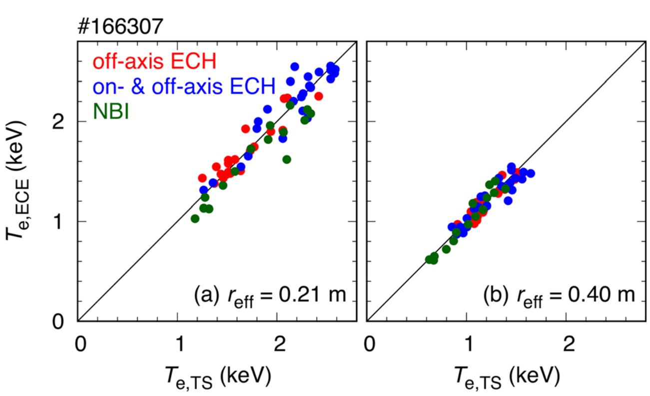

FIG. 6. Comparisons between T_e measured with ECE and T_e measured with TS at (a) $r_{eff} = 0.21$ m and (b) $r_{eff} = 0.40$ m for three different heating phases with only off-axis ECH, on- and off-axis ECH, and tangential NBI.

measured with TS during ECH phases, probably due to relatively high n_e, in terms of the effect of non-thermal electrons.[41] For reference, the effect of non-thermal electrons on ECE signals for this discharge is discussed in Appendix C.

The radial profile of q_e was directly evaluated from the energy conservation equation given by

$$q_e = \frac{1}{S}\int_0^{r_{eff}} dV\left(P_{ECH} + P_{NBI,e} - P_{e\to i} - n_e\frac{\partial T_e}{\partial t}\right),$$

where $P_{NBI,e}$ and $P_{e\to i}$ denote the electron heating power density by NBI and thermal relaxation power density from electrons to ions, respectively; S and V denote the surface area and the volume inside the flux surface at r_{eff}, respectively. It is noted that the radiation power density is omitted, because it is negligibly small in the analysis region. Since perpendicular NBI mainly heats ions, $P_{NBI,e}$ is negligibly small during the MECH period where tangential NBI heating is absent. The electron temperature gradient was calculated by the finite difference. The ion temperature was calculated by linear inter- and extrapolation of the measured T_i with CXS. Then, q_e/n_e and $-\nabla T_e$ were evaluated under the conditional average during on-axis MECH, as shown in Fig. 7. The conditional-averaged T_e also shows that the T_e profile became peaked after on-axis MECH was turned on and became hollow after on-axis MECH was turned off. During the turn-off phase, the negative $-\nabla T_e$ was formed between the on-axis MECH location and the off-axis ECH location. After on-axis MECH was turned on, $-\nabla T_e$ changed rapidly from negative to positive. Then, the flux-gradient relation was evaluated, as shown in Fig. 8. At $r_{eff} = 0.21$ m, where the negative $-\nabla T_e$ was formed in the off-axis ECH period, the q_e curve crossed two positive y-intercepts in the graph during the turn-on/off phases of on-axis MECH. This means two different values of q_e at zero $-\nabla T_e$. At the same time, two different values of q_e were observed in the flux-temperature diagram as shown in Fig. 8(b). This transport hysteresis phenomenon experimentally indicates the non-locality of the non-diffusion term in counter-gradient electron thermal transport. Dynamic transport behavior between positive and negative $-\nabla T_e$ was observed. It seems that the abrupt changes of q_e at the turn-on/off timings of on-axis MECH, i.e., the hysteresis widths, show an asymmetric property, although the cause is unclear at the moment.

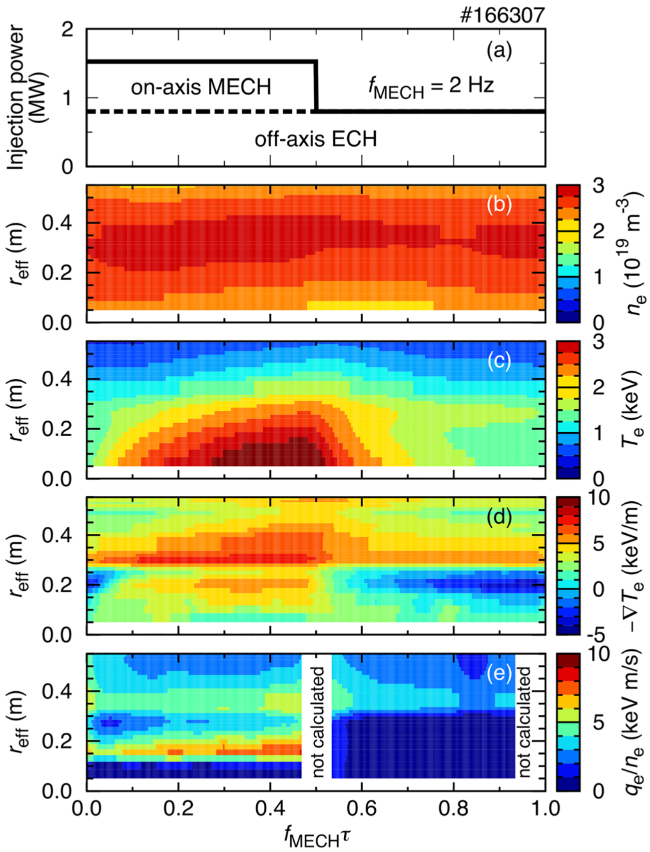

FIG. 7. Time evolution of the (a) injection power of ECH, radial profiles of (b) n_e, (c) T_e, (d) $-\nabla T_e$, and (e) q_e/n_e under conditional averaging during on-axis MECH.

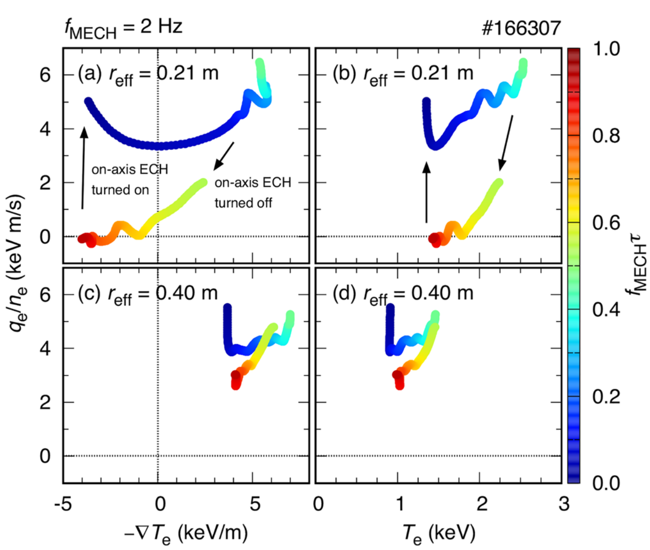

FIG. 8. Diagrams of the flux-gradient relation at (a) $r_{eff} = 0.21$ m and (c) $r_{eff} = 0.40$ m along with (b) and (d) the flux-temperature relation at same locations.

On the other hand, the flux-gradient and flux-temperature diagrams at $r_{eff} = 0.40$ m outside the off-axis ECH location show hysteresis trajectories in the region of positive $-\nabla T_e$ throughout the MECH period as shown in Figs. 8(c) and 8(d).

Figure 9 shows the radial profiles of the hysteresis widths $\Delta(q_e/n_e)$. The normalized electron heat flux q_e/n_e was averaged for $-\nabla T_e$ or for T_e during the turn-on/off phases of on-axis MECH, respectively. Then, $\Delta(q_e/n_e)$ was evaluated by subtracting the averaged q_e/n_e of the turn-off phase from that of the turn-on phase. The hysteresis widths are plotted in $r_{eff} > 0.2$ m, where on-axis MECH power deposition is almost absent. Therefore, uncertainty in the ECH deposition profile calculation need not to be accounted for. The result shows that normalized $\Delta(q_e/n_e)$ remains relatively large until the off-axis ECH location of $r_{eff} \sim 0.3$ m, being apart from the on-axis MECH location, and that normalized $\Delta(q_e/n_e)$ decreases outside the off-axis ECH location.

IV. DISCUSSIONS

A. Hollow electron temperature profiles

In Sec. I, we mention hollow T_e profiles in the RTP tokamak and the outward heat convection used to explain them.. However, RTP also explained some cases of hollow T_e profiles in the presence of low-order rational q surfaces and localized regions of greatly reduced diffusivity,[42] where q denotes the safety factor. Here, in the LHD, we do not think that the observed hollow T_e profiles relate to ι profiles, where ι denotes the rotational transform, because significant plasma current change was not observed in the off-axis ECH case (#165695) compared to the on-axis ECH case (#165692). The plasma current was less than 5 kA during the ECH pulse, i.e., almost current-less plasma. The ι profile inside $r_{eff}/a_{99} = 0.5$ is in a range of $1/3 < \iota/2\pi < 1/2$, but significant MHD (magnetohydrodynamics) activities were not observed in both discharges. We know that reduced diffusivity causes electron ITB (internal transport barrier) formation when strong on-

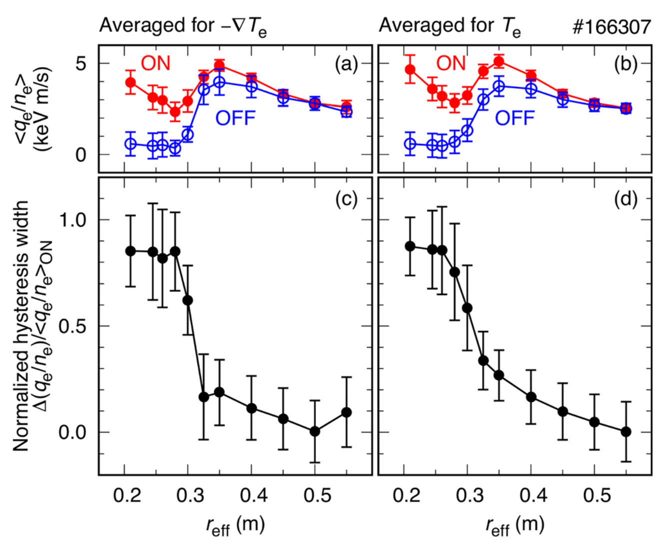

FIG. 9. Radial profiles of q_e/n_e averaged for (a) $-\nabla T_e$ or for (b) T_e during turn-on/off phases of on-axis MECH, and (c) and (d) hysteresis widths $\Delta(q_e/n_e)$ normalized by q_e/n_e of the turn-on phase of on-axis MECH.

axis ECH is applied to a relatively low-n_e plasma,[43] but adjusting the magnitude of the diffusion term does not contribute to the formation of the hollow T_e profile in the off-axis ECH case.

B. Hysteresis width

A similar description of the observed hysteresis is given in a DIII-D tokamak.[12] This reference notes that one explanation for the apparent hysteresis would be that the actual ECH deposition is significantly broader than predicted by a deposition code. We have already evaluated the effect of broadening ECH deposition profiles on the hysteresis width $\Delta(q_e/n_e)$.[25,44] The deposition profile that makes the hysteresis width zero can be caused by unreasonable misalignment in the steering antenna setting. Reasonable broadening of the deposition profile that accounts for oblique propagation of EC waves reduces q_e by $\sim$20% at observation radius, where the heating absorption is less significant. However, the qualitative hysteresis feature of q_e is still preserved, because q_e rapidly changes in response of heating in comparison to a continuous change of $-\nabla T_e$.

The abrupt changes of q_e at on-axis MECH turn-on/off, i.e., the hysteresis widths, are suggested to be associated with turbulent transport properties.[45] The immediate impact of heating power on turbulent transport is discussed in a theoretical model.[46] The change in the heating power can directly amplify the long-range fluctuation amplitude. The fluctuation amplitude is predicted to be

$$I = \frac{I_0}{1-\gamma_h \chi_0^{-1} k_\perp^{-2}},$$

where χ_0 and $k_\perp$ denote the turbulent diffusivity and the wavenumber of the fluctuation, respectively, and $\gamma_h \equiv \partial P_{ECH}/\partial p_e$ is the parameter of the direct impact of the heating power on the fluctuation amplitude. Here, p_e denotes the electron pressure. The fluctuation amplitude I_0 in the absence of heating is amplified to I after the onset of heating. The fluctuation can be enhanced at $\gamma_h \sim \chi_0 k_\perp^2$. Thanks to the fast change in γ_h, the turbulence amplitude and the electron heat flux can vary in advance of changes in local plasma parameters. For oblique propagation of a 154-GHz EC wave, an ECH absorption model is used to evaluate the heating efficiency.[25,47] Figure 10 shows the dependence of $\partial P_{ECH}/\partial p_e$ on T_e and n_e. Regardless of the evaluated locations, apart from the on-axis MECH location, $\partial P_{ECH}/\partial p_e \ll 1$ s^{-1} at $P_{ECH} \sim 1$ MW/m^3. In the plasma parameter range of discharge #166307, the ECH power was almost fully absorbed due to relatively high T_e and high n_e. The largest possible magnitude of the transport hysteresis is the case with $\chi_0 \sim 1$ m^2/s and $k_\perp \sim 5$ m^{-1} for $m=1$ global fluctuation in the LHD as the upper limit.[25] Thus, $\gamma_h \chi_0^{-1} k_\perp^{-2} \sim 0$. The model predicts no hysteresis due to relatively high T_e and high n_e during on-axis MECH of this discharge, although the model predicts that decreasing T_e and n_e enhances the hysteresis width in the turbulent thermal transport. It is unclear that this type of fluctuation was amplified by on-axis MECH in our case. We tried to compare the hysteresis width of q_e with the hysteresis widths of electron density fluctuations $\tilde{n}_e$ in experiments. Ions and electron scale turbulence were measured with two-dimensional phase contrast imaging and W-band millimeter-wave backscattering diagnostics.[48–50] However, a positive correlation of the hysteresis widths between q_e and $\tilde{n}_e$ has not been found at present, which should be clarified in future studies.

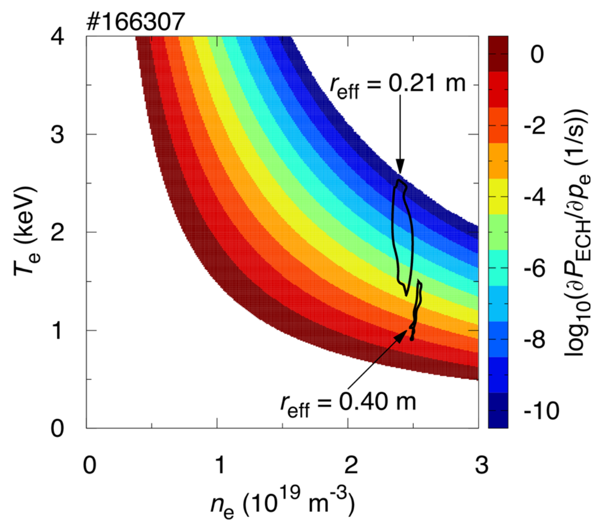

FIG. 10. Dependence of $\partial P_{ECH}/\partial p_e$ on T_e and n_e at $r_{eff} = 0.21$ and 0.40 m during on-axis MECH.

C. Neoclassical transport

The simple model to describe q_e, including diffusion and convection, is presented in Sec. III A. Here, neoclassical heat transport is compared with the model. Neoclassical transport was evaluated with the code "GSRAKE"[51] for the on-axis ECH and off-axis ECH cases. The two discharges for these cases are the same as shown in Figs. 2(a) and 2(d) for on-axis ECH and (c) and (f) for off-axis ECH. The neoclassical particle flux Γ_e and heat flux q_e for electrons are given by

$$\begin{aligned}\Gamma_e &= -D_1 n_e \left\{\frac{1}{n_e}\frac{\partial n_e}{\partial r} + \frac{eE_r}{T_e} + \left(\frac{D_2}{D_1} - \frac{3}{2}\right)\frac{1}{T_e}\frac{\partial T_e}{\partial r}\right\} \\ &\equiv -D_e \frac{\partial n_e}{\partial r} + V_e n_e, \\ q_e &= -D_2 n_e T_e \left\{\frac{1}{n_e}\frac{\partial n_e}{\partial r} + \frac{eE_r}{T_e} + \left(\frac{D_3}{D_2} - \frac{3}{2}\right)\frac{1}{T_e}\frac{\partial T_e}{\partial r}\right\} \\ &\equiv -n_e \chi_e \frac{\partial T_e}{\partial r} + n_e U_e T_e,\end{aligned}$$

where D_1, D_2, and D_3 are coefficients and E_r is the ambipolar radial electric field at $\Gamma_e(E_r) = \Gamma_i(E_r)$ for deuterium plasmas. Both Γ_e and q_e are modeled here as summation of the diffusion term and the non-diffusion term. Each diffusion term is proportional to $-\nabla n_e$ or $-\nabla T_e$. Each non-diffusion term is not proportional to the gradients and is expressed as the convection term. Here, D_e, V_e, χ_e, and U_e denote the electron particle diffusivity, the electron particle convection velocity, the electron heat diffusivity, and the electron heat convection velocity in neoclassical transport, respectively. Figure 11 shows the result of the neoclassical transport calculations. Here, the radial profiles of T_e, T_i, and n_e are fitted curves by polynomial functions of the tenth degree into the measured data. The normalized minor radius ρ is defined as $\rho \equiv r_{eff}/a_{99}$. This result in both cases shows that neoclassical electron particle transport is mainly convective, and neoclassical electron heat transport is mainly diffusive. Since the n_e profile is slightly hollow, the $-\nabla n_e$ contribution to the electron particle diffusion and the electron heat convection is relatively smaller.

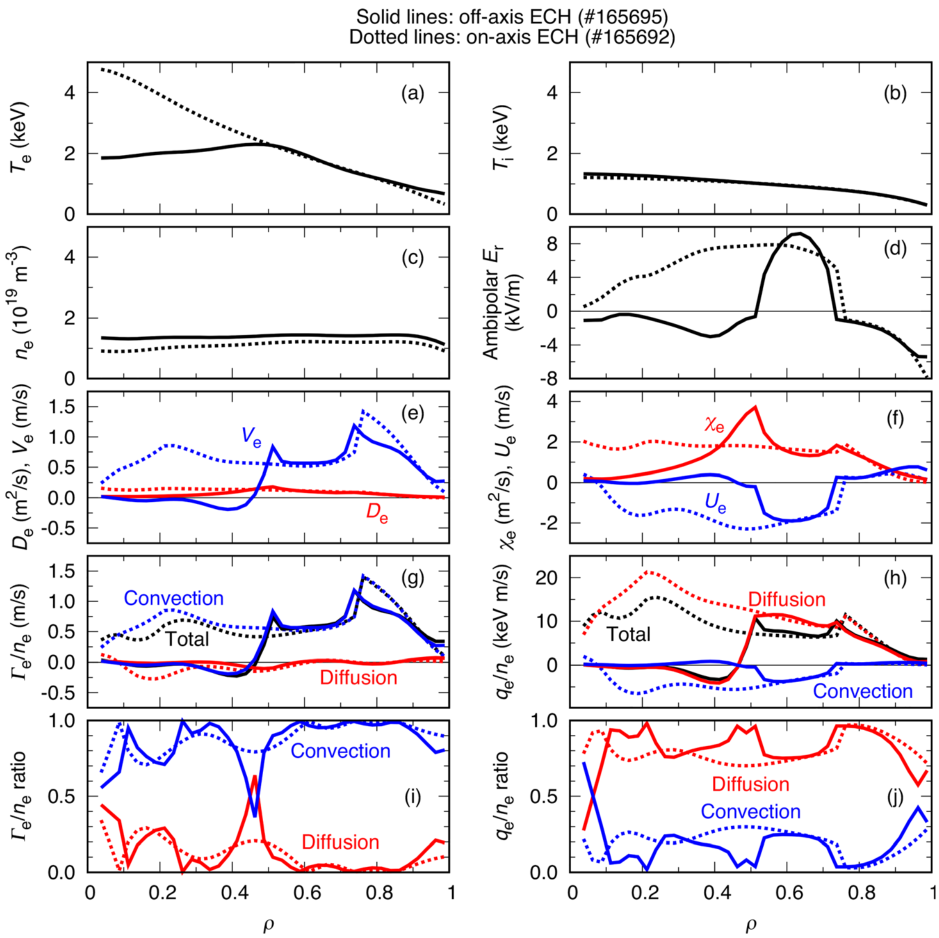

FIG. 11. Radial profiles of (a) T_e, (b) T_i, (c) n_e, (d) ambipolar E_r, (e) D_e, V_e, (f), χ_e, U_e, (g) Γ_e/n_e, (h) q_e/n_e, (i) ratio between the diffusion term and the convection term in the electron particle flux, and (j) ratio between the diffusion term and the convection term in the electron heat flux in cases of off-axis ECH and on-axis ECH, calculated with the neoclassical transport code GSRAKE.

On the other hand, the positive $-\nabla T_e$ in the whole region of the on-axis EC heated plasma and in the outer region of the off-axis ECH location mainly contribute to outward particle convection and outward heat diffusion. Additionally, in the region of the positive ambipolar E_r (the electron root) in both cases, the generated inward U_e slightly increases the ratio of the convective q_e/n_e up to $\sim$30%. Neoclassical transport behavior is similar in both cases outside the off-axis ECH location of $\rho \sim 0.5$, because the radial profiles of T_e, T_i, and n_e are similar in both cases. On the other hand, in the negative $-\nabla T_e$ region of the hollow T_e profile in the off-axis ECH case, both Γ_e/n_e and q_e/n_e are much smaller than those in the positive $-\nabla T_e$ region of the peaked T_e profile in the on-axis ECH case. In contrast to the positive ambipolar E_r at $\rho \lesssim 0.7$ in the on-axis ECH case, the negative ambipolar E_r (the ion root) is obtained inside the off-axis ECH location of $\rho \sim 0.5$. The transition from the electron root to the ion root is observed, in contrast to the inverse transition at the formation of electron ITB, where the strong positive $-\nabla T_e$ is generated.[43] This transition from the large positive E_r to the slightly negative E_r contributes to changing the U_e direction from negative to positive. However, the generated outward heat convection is insufficient to compensate for inward heat diffusion in the negative $-\nabla T_e$ region. Thus, net inward q_e/n_e is present around $\rho \sim 0.4$. The ratio of the neoclassical convective q_e/n_e is only less than 30% at $0.1 \lesssim \rho \lesssim 0.5$ inside the off-axis ECH location, although the modeled inward diffusive q_e/n_e and outward convective q_e/n_e cancel each other, as shown in Fig. 3. The average value of neoclassical χ_e and U_e inside the off-axis ECH location is 0.9 m^2/s and 0.1 m/s, respectively. This order is comparable to the estimated $\chi_e(= 0.70$ m^2/s) and $U_e(= 0.58$ m/s) with the model written in Sec. III A. It should be noted that there is an ion root in $0.53 < \rho < 0.72$ in the off-axis ECH case, although the electron root is selected because the ion root gives rise to unreasonable q_e/n_e much larger than that shown in Fig. 3, whose model uses the real ECH power input. Thus, the neoclassical q_e/n_e less than 10 keV m/s can be obtained, although the U_e direction is opposite to the modeled one there.

V. SUMMARY

The direct observation of the non-locality of the non-diffusion term in transient electron thermal transport, associated with outward heat convection, was successfully performed in the condition that on-axis MECH was applied to the plasma sustained by off-axis ECH. In this experiment, the on-axis MECH power and off-axis ECH power were comparable so that the dynamic transport behavior between positive and negative gradient regions was observed in the transport hysteresis phenomenon. One other item of interest would be a case where the off-axis ECH power is much larger than the on-axis ECH power. Suppose the steady-state negative gradient on the electron temperature ($-\nabla T_e < 0$) can be formed, even under steady-state on-axis ECH, together with steady-state off-axis ECH. In that case, the steady-state significant positive electron heat flux is expected in counter-gradient electron thermal transport, where radiation loss, as well as thermal relaxation to ions, can be neglected, compared to the on-axis ECH power density. This type of experiment will promote building a model for non-diffusive counter-gradient transport.

ACKNOWLEDGMENTS

The authors acknowledge all the members of the LHD Experiment Group for their assistance. The authors are grateful to Professor S. Inagaki of Kyushu University for valuable discussions. This work was partly supported by the National Institute for Fusion Science under Grant No. KLPH038.

AUTHOR DECLARATIONS

Conflict of Interest

The authors have no conflicts of interest to disclose.

DATA AVAILABILITY

The data that support the findings of this study are available from the corresponding author upon reasonable request. The data that support the findings of this study are openly available in LHD data repository at https://www-lhd.nifs.ac.jp/pub/Repository_en.html, Ref. 53.

APPENDIX A: ELECTRON DENSITY PROFILE DURING MECH

The n_e profile was almost unchanged during MECH. The reason is discussed in terms of the ECH-driven neoclassical particle flux. The description of the GSRAKE code is found in Sec. IV C. Figure 12 shows a result of neoclassical transport calculations with the GSRAKE code in the MECH experiment at 4.700 s on the off-axis ECH phase and at 4.466 s on the on- and off-axis ECH phase. On-axis ECH changes the T_e profile from hollow to peaked, while the n_e profile is almost unchanged. Due to the lack of T_i measurement at 4.466 s, the T_i profile at 4.466 s is given as the same as that at 4.700 s. The ambipolar E_r at the off-axis ECH phase is slightly smaller than that at the on- and off-axis ECH phase. The main contribution to the changes of V_e and χ_e is caused by the $-\nabla T_e$ change.

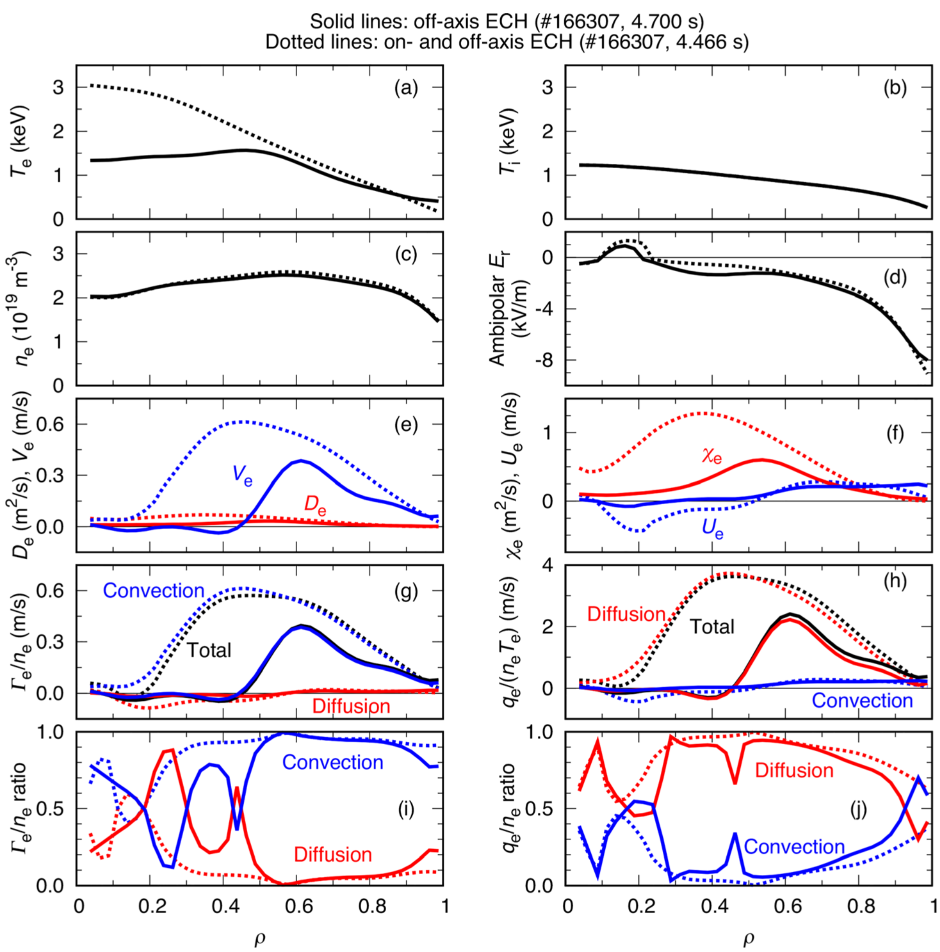

FIG. 12. Radial profiles of (a) T_e, (b) T_i, (c) n_e, (d) ambipolar E_r, (e) D_e, V_e, (f) χ_e, U_e, (g) Γ_e/n_e, (h) $q_e/(n_e T_e)$, (i) ratio between the diffusion term and the convection term in the electron particle flux, and (j) ratio between the diffusion term and the convection term in the electron heat flux in cases of off-axis ECH and on- and off-axis ECH, calculated with the GSRAKE code.

Surely, $-\nabla T_e$ directly affects the neoclassical particle transport. However, the time scales of particle transport and heat transport are different. The timescale on the electron particle flux, $a_{99}/(\Gamma_e/n_e T_e)$, is at least five times longer than that on the electron heat flux, $a_{99}/(q_e/n_e)$, in $0.5 < \rho < 0.9$ for the off-axis ECH case and in $0.3 < \rho < 0.9$ for the on- and off-axis ECH case. Here, $a_{99} = 0.61$ m. The particle confinement time, $\tau_p = \int_V n_e dV / \oint_A \Gamma_e dA$, is estimated to be $\tau_p = 1.2$ s for the off-axis ECH case and $\tau_p = 0.9$ s for the on- and off-axis ECH case, which are longer than the modulation half period of 0.25 s. Here, A denotes the plasma surface area, normally defined at the last closed flux surface (LCFS, $\rho = 1$). However, neoclassical $\oint_{A(\rho)} \Gamma_e dA(\rho)$ decreases toward the LCFS. Thus, we evaluate it at $\rho = 0.64$, where the maximum $\oint_{A(\rho)} \Gamma_e dA(\rho)$ can be obtained. The above evaluation suggests that the n_e profile is almost unchanged by the change of the ECH-driven neoclassical particle flux during MECH, compared to the fast change in the T_e profile.

APPENDIX B: CHANGE IN PLASMA STORED ENERGY

In the MECH experiment shown in Fig. 4, the plasma stored energy W_p decreases by 35% at most after turning off the on-axis MECH. Figure 13 shows the time evolution of W_p in comparison to the ISS04 scaling (International Stellarator Scaling proposed in 2004).[52] Here, the plasma stored energy of ISS04, W_p^{ISS04}, at the steady state is given by

$$W_p^{ISS04} = P\tau_E^{ISS04} = 0.134 a^{2.28} R^{0.64} P^{0.39} \bar{n}_e^{0.54} B^{0.84} (\iota_{2/3}/2\pi)^{0.41},$$

where $a = 0.63$ m, $R = 3.6$ m, $\bar{n}_e = 2.3 \times 10^{19}$ m^{-3}, $B = 2.75$ T, $\iota_{2/3}/2\pi = 0.65$, $P = 1.52$ MW for the turn-on phase of on-axis MECH, and $P = 0.80$ MW for the turn-off phase of on-axis MECH. This result shows that the experimental W_p asymptotes to the ISS04 scaling during the turn-on phase of on-axis MECH, while the experimental W_p decreases worse than the scaling. The scaling of $W_p^{ISS04} \propto P^{0.39}$ cannot explain 35% reduction of the experimental W_p. The line-averaged n_e, the n_e profiles, and the parameters related to the scaling did not appear to change during the MECH period. This result suggests that hollow T_e profiles with off-axis ECH degrade the plasma confinement, relaxing the state beneath the scaling. Nevertheless, experimental data in wide ranges of the scaling parameters should be accumulated to discuss the confinement property of LHD plasmas with hollow T_e profiles.

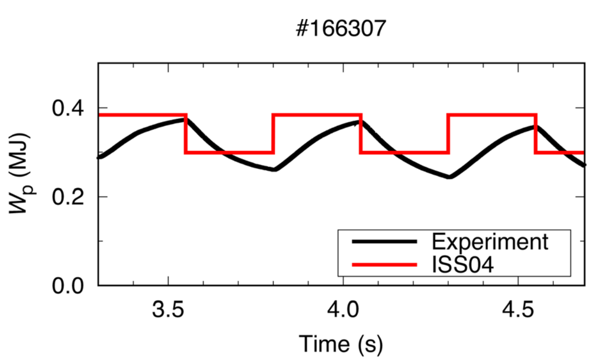

FIG. 13. Time evolution of W_p compared to the ISS04 scaling.

APPENDIX C: EFFECT OF NON-THERMAL ELECTRONS

The effect of non-thermal electrons is more or less included in ECE signals, especially near the core, while the TS diagnostic is less sensitive to non-thermal electrons. The diamagnetic loop measures all contributions in principle. Figure 14 shows the time evolution of the diamagnetic stored energy $W_{p,dia}$ in comparison to the kinetic stored energy in the MECH experiment. The diamagnetic stored energy is the same as shown in Fig. 4(c). Here, the electron kinetic stored energy W_{pe} was estimated by integrating the product of n_e and T_e by the plasma volume. Regarding the ion kinetic stored energy W_{pi}, we assumed that impurity carbon ions C^{6+} were included in the deuterium plasma due to carbon divertor plates in the LHD. The deuterium ion density and the carbon ion density were obtained from Z_{eff} and charge neutrality, respectively. The ion temperature T_i was measured with CXS and short-pulse diagnostic perpendicular NBI at 4.7 and 6.5 s only, so that T_i during the ECH phase was assumed to be the same as T_i at 4.7 s, and T_i during the tangential NBI phase was linearly interpolated with T_i at the two timings.

During the MECH phase (from 3.3 to 4.8 s), we are focusing on in this paper, $2W_{pe}$ was overestimated due to $T_e > T_i$, while $W_{pe} + W_{pi}$ was lower than $W_{p,dia}$ by 20% at most. During the tangential NBI phase (from 5.1 s), even $2W_{pe}$ was lower than $W_{p,dia}$ although still $T_e > T_i$ in the whole region. In addition, $W_{pe} + W_{pi}$ was much lower than $W_{p,dia}$. These results imply that non-thermal electrons during the MECH phase and high-energy ions during the tangential NBI phase give rise to anisotropic pressure that contributes to the diamagnetic loop measurement. On the other hand, during another ECH phase (from 4.8 to 5.1 s) connected between the MECH phase and the tangential NBI phase in this discharge, $W_{pe} + W_{pi}$ was close to $W_{p,dia}$ at 5.1 s where heating was switched from ECH to NBI. The slowing down time of high-energy electrons due to collisions with bulk electrons is estimated, and it is ~20 ms

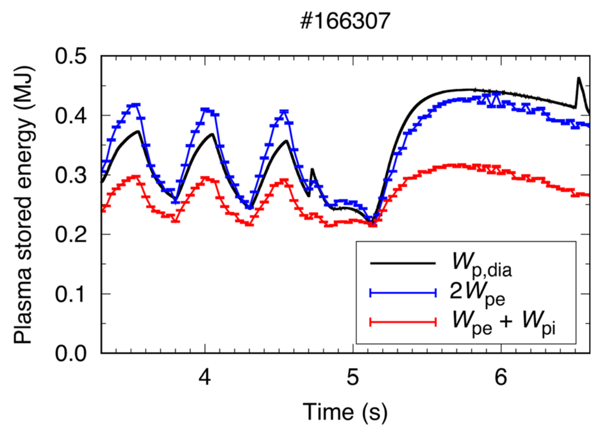

FIG. 14. Time evolution of diamagnetic stored energy in comparison to kinetic stored energy.

for electrons at half the speed of light. Thus, the effect of non-thermal electrons is expected to disappear quickly, and high-energy ions are expected to be few at 5.1 s.

Nevertheless, the diamagnetic stored energy is generally influenced by the plasma current, volume change with the finite β effect, and high-energy charged particles. Therefore, in order to verify the effect of non-thermal electrons specifically, comparisons between diamagnetic and kinetic stored energy should be carefully and statistically investigated, such as in a wide range of the electron density, heating power, plasma current, and plasma volume, which we believe is beyond the scope of this paper.

Although we expect that non-thermal electrons change diamagnetic stored energy and may have possibility to change ECE spectra, in general, at the on-axis ECH location, at least T_e measured with the ECE diagnostic, which was calibrated with the TS diagnostic during the tangential NBI phase, was in good agreement with T_e measured with TS within 20% both in the tangential NBI phase and in the MECH phase, at the outside of the on-axis MECH location, e.g., at $r_{eff} = 0.21$ and 0.40 m, where the electron heat flux was evaluated. Thus, this evidence does not change the conclusion through evaluating the electron heat flux presented in this paper.

REFERENCES

[1] T. C. Luce, C. C. Petty, and J. G. Cordey, Plasma Phys. Controlled Fusion **50**, 043001 (2008).
[2] G. R. Tynan, A. Fujisawa, and G. McKee, Plasma Phys. Controlled Fusion **51**, 113001 (2009).
[3] H. Yamada, K. Tanaka, R. Seki, C. Suzuki, K. Ida, K. Fujii, M. Goto, S. Murakami, M. Osakabe, T. Tokuzawa, M. Yokoyama, M. Yoshinuma, and LHD Experiment Group, Phys. Rev. Lett. **123**, 185001 (2019).
[4] J. Garcia, R. J. Dumont, J. Joly, J. Morales, L. Garzotti, T. W. Bache, Y. Baranov, F. J. Casson, C. Challis, K. Kirov, J. Mailloux, S. Saarelma, M. Nocente, A. Banon-Navarro, T. Goerler, J. Citrin, A. Ho, D. Gallart, M. Mantsinen, and JET Contributors, Nucl. Fusion **59**, 086047 (2019).
[5] P. A. Schneider, A. Bustos, P. Hennequin, F. Ryter, M. Bernert, M. Cavedon, M. G. Dunne, R. Fischer, T. Görler, T. Happel, V. Igochine, B. Kurzan, A. Lebschy, R. M. McDermott, P. Morel, M. Willensdorfer, ASDEX Upgrade Team, and EUROfusion MST1 Team, Nucl. Fusion **57**, 066003 (2017).
[6] C. F. Maggi, H. Weisen, J. C. Hillesheim, A. Chankin, E. Delabie, L. Horvath, F. Auriemma, I. S. Carvalho, G. Corrigan, J. Flanagan, L. Garzotti, D. Keeling, D. King, E. Lerche, R. Lorenzini, M. Maslov, S. Menmuir, S. Saarelma, A. C. C. Sips, E. R. Solano, E. Belonohy, F. J. Casson, C. Challis, C. Giroud, V. Parail, C. Silva, M. Valisa, and JET Contributors, Plasma Phys. Controlled Fusion **60**, 014045 (2018).
[7] K. Ida and T. Fujita, Plasma Phys. Controlled Fusion **60**, 033001 (2018).
[8] T. Kobayashi, H. Takahashi, K. Nagaoka, M. Sasaki, M. Nakata, M. Yokoyama, R. Seki, M. Yoshinuma, and K. Ida, Sci. Rep. **9**, 15913 (2019).
[9] K. W. Gentle, W. L. Rowan, R. V. Bravenec, G. Cima, T. P. Crowley, H. Gasquet, G. A. Hallock, J. Heard, A. Ouroua, P. E. Phillips, D. W. Ross, P. M. Schoch, and C. Watts, Phys. Rev. Lett. **74**, 3620 (1995).
[10] J. D. Callen and M. W. Kissick, Plasma Phys. Controlled Fusion **39**, B173 (1997).
[11] P. Mantica, G. Gorini, G. M. D. Hogeweij, N. J. Lopes Cardozo, and A. M. R. Schilham, Phys. Rev. Lett. **85**, 4534 (2000).
[12] K. W. Gentle, M. E. Austin, J. C. DeBoo, T. C. Luce, and C. C. Petty, Phys. Plasmas **13**, 012311 (2006).
[13] K. Ida, Z. Shi, H. J. Sun, S. Inagaki, K. Kamiya, J. E. Rice, N. Tamura, P. H. Diamond, G. Dif-Pradalier, X. L. Zou, K. Itoh, S. Sugita, O. D. Gürcan, T. Estrada, C. Hidalgo, T. S. Hahm, A. Field, X. T. Ding, Y. Sakamoto, S. Oldenbürger, M. Yoshinuma, T. Kobayashi, M. Jiang, S. H. Hahn, Y. M. Jeon, S. H. Hong, Y. Kosuga, J. Dong, and S.-I. Itoh, Nucl. Fusion **55**, 013022 (2015).
[14] X. Q. Ji, Y. Xu, C. Hidalgo, P. H. Diamond, Y. Liu, O. Pan, Z. B. Shi, and D. L. Yu, Sci. Rep. **6**, 32697 (2016).
[15] P. Rodriguez-Fernandez, A. E. White, N. T. Howard, B. A. Grierson, G. M. Staebler, J. E. Rice, X. Yuan, N. M. Cao, A. J. Creely, M. J. Greenwald, A. E. Hubbard, J. W. Hughes, J. H. Irby, and F. Sciortino, Phys. Rev. Lett. **120**, 075001 (2018).
[16] B. P. van Milligen, B. A. Carreras, L. García, A. Martín de Aguilera, C. Hidalgo, J. H. Nicolau, and TJ-II Team, Phys. Plasmas **23**, 072307 (2016).
[17] S. Ding, B. Wan, L. Wang, A. Ti, X. Zhang, Z. Liu, J. Qian, G. Zhong, and Y. Duan, Plasma Sci. Technol. **16**, 826 (2014).
[18] C. C. Petty and T. C. Luce, Nucl. Fusion **34**, 121 (1994).
[19] S. D. Song, X. L. Zou, G. Giruzzi, W. W. Xiao, X. T. Ding, B. J. Ding, J. L. Ségui, D. Elbèze, F. Clairet, C. Fenzi, T. Aniel, J. F. Artaud, V. Basiuk, F. Bouquey, R. Magne, E. Corbel, and Tore Supra Team, Nucl. Fusion **52**, 033006 (2012).
[20] P. Mantica, A. Thyagaraja, J. Weiland, G. M. D. Hogeweij, and P. J. Knight, Phys. Rev. Lett. **95**, 185002 (2005).
[21] K. Nagasaki, T. Mizuuchi, S. Besshou, H. Funaba, K. Ida, K. Kondo, H. Morioka, T. Obiki, H. Okada, F. Sano, and H. Zushi, J. Phys. Soc. Jpn. **67**, 1625 (1998).
[22] H. Renner, W7AS Team, NBI Group, ICF Group, and ECRH Group, Plasma Phys. Controlled Fusion **31**, 1579 (1989).
[23] U. Stroth, L. Giannone, H.-J. Hartfuss, ECH Group, and W7-AS Team, Plasma Phys. Controlled Fusion **38**, 611 (1996).
[24] T. Kobayashi, K. Ida, K. Tanaka, M. Yoshinuma, T. Ii Tsujimura, S. Inagaki, T. Tokuzawa, H. Tsuchiya, N. Tamura, H. Igami, Y. Yoshimura, S.-I. Itoh, K. Itoh, and LHD Experiment Group, Nucl. Fusion **60**, 076015 (2020).
[25] T. Kobayashi, K. Ida, T. Ii Tsujimura, S. Inagaki, T. Tokuzawa, H. Tsuchiya, N. Tamura, H. Igami, Y. Yoshimura, S.-I. Itoh, K. Itoh, and LHD Experiment Group, Nucl. Fusion **58**, 126031 (2018).
[26] M. van Berkel, G. Vandersteen, H. J. Zwart, G. M. D. Hogeweij, J. Citrin, E. Westerhof, D. Peumans, and M. R. de Baar, Nucl. Fusion **58**, 106042 (2018).
[27] Y. Takeiri, T. Morisaki, M. Osakabe, M. Yokoyama, S. Sakakibara, H. Takahashi, Y. Nakamura, T. Oishi, G. Motojima, S. Murakami, K. Ito, A. Ejiri, S. Imagawa, S. Inagaki, M. Isobe, S. Kubo, S. Masamune, T. Mito, I. Murakami, K. Nagaoka, K. Nagasaki, K. Nishimura, M. Sakamoto, R. Sakamoto, T. Shimozuma, K. Shinohara, H. Sugama, K. Y. Watanabe, J. W. Ahn, N. Akata, T. Akiyama, N. Ashikawa, J. Baldzuhn, T. Bando, E. Bernard, F. Castejón, H. Chikaraishi, M. Emoto, T. Evans, N. Ezumi, K. Fujii, H. Funaba, M. Goto, T. Goto, D. Gradic, Y. Gunsu, S. Hamaguchi, H. Hasegawa, Y. Hayashi, C. Hidalgo, T. Higashiguchi, Y. Hirooka, Y. Hishinuma, R. Horiuchi, K. Ichiguchi, K. Ida, T. Ido, H. Igami, K. Ikeda, S. Ishiguro, R. Ishizaki, A. Ishizawa, A. Ito, Y. Ito, A. Iwamoto, S. Kamio, K. Kamiya, O. Kaneko, R. Kanno, H. Kasahara, D. Kato, T. Kato, K. Kawahata, G. Kawamura, M. Kisaki, S. Kitajima, W. H. Ko, M. Kobayashi, S. Kobayashi, T. Kobayashi, K. Koga, A. Kohyama, R. Kumazawa, J. H. Lee, D. López-Bruna, R. Makino, S. Masuzaki, Y. Matsumoto, H. Matsuura, O. Mitarai, H. Miura, J. Miyazawa, N. Mizuguchi, C. Moon, S. Morita, T. Moritaka, K. Mukai, T. Muroga, S. Muto, T. Mutoh, T. Nagasaka, Y. Nagayama, N. Nakajima, Y. Nakamura, H. Nakanishi, H. Nakano, M. Nakata, Y. Narushima, D. Nishijima, A. Nishimura, S. Nishimura, T. Nishitani, M. Nishiura, Y. Nobuta, H. Noto, M. Nunami, T. Obana, K. Ogawa, S. Ohdachi, M. Ohno, N. Ohno, H. Ohtani, M. Okamoto, Y. Oya, T. Ozaki, B. J. Peterson, M. Preynas, S. Sagara, K. Saito, H. Sakaue, A. Sanpei, S. Satake, M. Sato, T. Saze, O. Schmitz, R. Seki, T. Seki, I. Sharov, A. Shimizu, M. Shiratani, M. Shoji, C. Skinner, R. Soga, T. Stange, C. Suzuki, Y. Suzuki, S. Takada, K. Takahata, A. Takayama, S. Takayama, Y. Takemura, Y. Takeuchi, H. Tamura, N. Tamura, H. Tanaka, K. Tanaka, M. Tanaka, T. Tanaka, Y. Tanaka, S. Toda, Y. Todo, K. Toi, M. Toida, M. Tokitani, T. Tokuzawa, H. Tsuchiya, T. Tsujimura, K. Tsumori, S. Usami, J. L. Velasco, H. Wang, T.-H. Watanabe, T. Watanabe, J. Yagi, M. Yajima, H. Yamada, I. Yamada, O. Yamagishi, N. Yamaguchi, Y. Yamamoto, N. Yanagi, R. Yasuhara, E. Yatsuka, N. Yoshida, M. Yoshinuma, S. Yoshimura, and Y. Yoshimura, Nucl. Fusion **57**, 102023 (2017).
[28] T. I. Tsujimura, R. Yanai, Y. Mizuno, K. Tanaka, Y. Yoshimura, T. Tokuzawa, M. Nishiura, R. Sakamoto, G. Motojima, S. Kubo, T. Shimozuma, H. Igami, H. Takahashi, M. Yoshinuma, S. Ohshima, and LHD Experiment Group, Nucl. Fusion **61**, 026012 (2021).
[29] C. Suzuki, K. Ida, Y. Suzuki, M. Yoshida, M. Emoto, and M. Yokoyama, Plasma Phys. Controlled Fusion **55**, 014016 (2013).

[30]T. I. Tsujimura, S. Kubo, H. Takahashi, R. Makino, R. Seki, Y. Yoshimura, H. Igami, T. Shimozuma, K. Ida, C. Suzuki, M. Emoto, M. Yokoyama, T. Kobayashi, C. Moon, K. Nagaoka, M. Osakabe, S. Kobayashi, S. Ito, Y. Mizuno, K. Okada, A. Ejiri, T. Mutoh, and LHD Experiment Group, Nucl. Fusion **55**, 123019 (2015).
[31]I. Yamada, H. Funaba, R. Yasuhara, H. Hayashi, N. Kenmochi, T. Minami, M. Yoshikawa, K. Ohta, J. H. Lee, and S. H. Lee, Rev. Sci. Instrum. **87**, 11E531 (2016).
[32]H. Tsuchiya, Y. Nagayama, K. Kawahata, S. Inagaki, S. Kubo, and LHD Experiment Group, Plasma Fusion Res. **6**, 2402114 (2011).
[33]T. Akiyama, K. Kawahata, K. Tanaka, T. Tokuzawa, Y. Ito, S. Okajima, K. Nakayama, C. A. Michael, L. N. Vyacheslavov, A. Sanin, S. Tsuji-Iio, and LHD Experiment Group, Fusion Sci. Technol. **58**, 352 (2010).
[34]M. Yoshinuma, K. Ida, M. Yokoyama, M. Osakabe, and K. Nagaoka, Fusion Sci. Technol. **58**, 375 (2010).
[35]M. Goto and S. Morita, Plasma Fusion Res. **5**, S1040 (2010).
[36]K. Mukai, S. Masuzaki, Y. Hayashi, T. Oishi, C. Suzuki, M. Kobayashi, H. Tanaka, B. J. Peterson, and LHD Experiment Group, Plasma Fusion Res. **15**, 1402051 (2020).
[37]Y. Kawamoto, S. Morita, M. Goto, and T. Oishi, Plasma Fusion Res. **16**, 2402072 (2021).
[38]K. Tanaka, Y. Ohtani, M. Nakata, F. Warmer, T. Tsujimura, Y. Takemura, T. Kinoshita, H. Takahashi, M. Yokoyama, R. Seki, H. Igami, Y. Yoshimura, S. Kubo, T. Shimozuma, T. Tokuzawa, T. Akiyama, I. Yamada, R. Yasuhara, H. Funaba, M. Yoshinuma, K. Ida, M. Goto, G. Motojima, M. Shoji, S. Masuzaki, C. A. Michael, L. N. Vacheslavov, M. Osakabe, and T. Morisaki, Nucl. Fusion **59**, 126040 (2019).
[39]K. Tanaka, K. Kawahata, T. Tokuzawa, T. Akiyama, M. Yokoyama, M. Shoji, C. A. Michael, L. N. Vyacheslavov, S. Murakami, A. Wakasa, A. Mishchenko, K. Muraoka, S. Okajima, H. Takenaga, and LHD Experiment Group, Fusion Sci. Technol. **58**, 70 (2010).
[40]Y. Ohtani, K. Tanaka, T. Tokuzawa, T. Akiyama, I. Yamada, R. Yasuhara, H. Funaba, M. Shoji, M. Goto, and LHD Experimental Group, Plasma Phys. Controlled Fusion **62**, 025029 (2020).
[41]S. Kubo, H. Takahashi, T. Shimozuma, Y. Yoshimura, M. Nishiura, H. Igami, S. Ogasawara, and R. Makino, EPJ Web Conf. **32**, 02007 (2012).
[42]G. M. D. Hogeweij, N. J. Lopes Cardozo, M. R. De Baar, and A. M. R. Schilham, Nucl. Fusion **38**, 1881 (1998).
[43]K. Ida, T. Shimozuma, H. Funaba, K. Narihara, S. Kubo, S. Murakami, A. Wakasa, M. Yokoyama, Y. Takeiri, K. Y. Watanabe, K. Tanaka, M. Yoshinuma, Y. Liang, N. Ohyabu, and LHD Experimental Group, Phys. Rev. Lett. **91**, 085003 (2003).
[44]T. Kobayashi, R. Yanai, T. I. Tsujimura, T. Tokuzawa, Y. Yoshimura, K. Ida, and LHD Experiment Group, Plasma Fusion Res. **15**, 1402072 (2020).
[45]S. Inagaki, T. Tokuzawa, N. Tamura, S.-I. Itoh, T. Kobayashi, K. Ida, T. Shimozuma, S. Kubo, K. Tanaka, T. Ido, A. Shimizu, H. Tsuchiya, N. Kasuya, Y. Nagayama, K. Kawahata, S. Sudo, H. Yamada, A. Fujisawa, K. Itoh, and LHD Experiment Group, Nucl. Fusion **53**, 113006 (2013).
[46]S.-I. Itoh and K. Itoh, Nucl. Fusion **53**, 073035 (2013).
[47]A. C. England, O. C. Eldridge, S. F. Knowlton, M. Porkolab, and J. R. Wilson, Nucl. Fusion **29**, 1527 (1989).
[48]K. Tanaka, C. A. Michael, L. N. Vyacheslavov, A. L. Sanin, K. Kawahata, T. Akiyama, T. Tokuzawa, and S. Okajima, Rev. Sci. Instrum. **79**, 10E702 (2008).
[49]C. A. Michael, K. Tanaka, L. Vyacheslavov, A. Sanin, and K. Kawahata, Rev. Sci. Instrum. **86**, 093503 (2015).
[50]T. Tokuzawa, K. Tanaka, T. Tsujimura, S. Kubo, M. Emoto, S. Inagaki, K. Ida, M. Yoshinuma, K. Y. Watanabe, H. Tsuchiya, A. Ejiri, T. Saito, K. Yamamoto, and LHD Experiment Group, Rev. Sci. Instrum. **92**, 043536 (2021).
[51]C. D. Beidler and W. D. D'haeseleer, Plasma Phys. Controlled Fusion **37**, 463 (1995).
[52]H. Yamada, J. H. Harris, A. Dinklage, E. Ascasibar, F. Sano, S. Okamura, J. Talmadge, U. Stroth, A. Kus, S. Murakami, M. Yokoyama, C. D. Beidler, V. Tribaldos, K. Y. Watanabe, and Y. Suzuki, Nucl. Fusion **45**, 1684 (2005).
[53]Large Helical Device Project, LHD Experiment Data Repository. https://www-lhd.nifs.ac.jp/pub/Repository_en.html.